Momentum transport studies from multi-machine comparisons

M. Yoshida[1], **S. Kaye**[2], **J. Rice**[3], **W. Solomon**[2], **T. Tala**[4], **R.E. Bell**[2],
K.H. Burrell[5], **J. Ferreira**[6], **Y. Kamada**[1], **D. McDonald**[7,8],
P. Mantica[9], **Y. Podpaly**[3], **M.L. Reinke**[3], **Y. Sakamoto**[1], **A. Salmi**[4]
and the ITPA Transport & Confinement Topical Group

[1] Japan Atomic Energy Agency, Naka, Ibaraki-ken 311-0193, Japan

[2] Princeton Plasma Physics Laboratory, Princeton University, Princeton, NJ 08543, USA

[3] Plasma Science and Fusion Center, MIT, Cambridge, MA 02139, USA

[4] Association EURATOM-Tekes, VTT, PO Box 1000, FIN-02044 VTT, Finland

[5] General Atomics, PO Box 85608, San Diego, CA 92186-5608, USA

[6] Associação EURATOM/IST, Instituto de Plasmas e Fusão Nuclear, Instituto Superior
Técnico, Universidade Técnica de Lisboa, 1049-001 Lisboa, Portugal

[7] Culham Centre for Fusion Energy, Abingdon, UK

[8] EFDA-CSU Garching, München, Germany

[9] Istituto di Fisica del Plasma CNR-EURATOM, via Cozzi 53, 20125 Milano, Italy

E-mail: yoshida.maiko@jaea.go.jp

Abstract

A database of toroidal momentum transport on five tokamaks, Alcator C-Mod, DIII-D, JET, NSTX and JT-60U, has been constructed under a wide range of conditions in order to understand the characteristics of toroidal momentum transport coefficients, namely the toroidal momentum diffusivity (χ_ϕ) and the pinch velocity (V_{pinch}). Through an inter-machine comparison, the similarities and differences in the properties of χ_ϕ and V_{pinch} among the machines have been clarified. Parametric dependences of these momentum transport coefficients have been investigated over a wide range of plasma parameters taking advantage of the different operation regimes in machines. The approach offers insights into the parametric dependences as follows. The toroidal momentum diffusivity (χ_ϕ) generally increases with increasing heat diffusivity (χ_i). The correlation is observed over a wide range of χ_ϕ, covering roughly two orders of magnitude, and within each of the machines over the whole radius. Through the inter-machine comparison, it is found that χ_ϕ becomes larger in the outer region of the plasma. Also observed is a general trend for V_{pinch} in tokamaks; the inward pinch velocity ($-V_{\text{pinch}}$) increases with increasing χ_ϕ. The results that are commonly observed in machines will support a toroidal rotation prediction in future devices. On the other hand, differences among machines have been observed. The toroidal momentum diffusivity, χ_ϕ, is larger than or equal to χ_i in JET and JT-60U; on the other hand, χ_ϕ is smaller than or equal to χ_i in NSTX, DIII-D and Alcator C-Mod. In DIII-D, the ratio $-RV_{\text{pinch}}/\chi_\phi$ at $r/a = 0.5$–0.6 is about 2, which is small compared with that in other tokamaks ($-RV_{\text{pinch}}/\chi_\phi \approx 5$). Based on these different observations, parametric dependences of χ_ϕ/χ_i, $RV_{\text{pinch}}/\chi_\phi$ and χ_ϕ have been investigated in H-mode plasmas. Across the dataset from all machines, the ratio χ_ϕ/χ_i tends to be larger in low ν_e^* at fixed T_e/T_i and ρ_{pol}^*. An increase in χ_ϕ is observed with decreasing n_e and/or increasing T_e. The pinch number ($-RV_{\text{pinch}}/\chi_\phi$) is observed to increase with increasing R/L_{n_e} at both $q_{95} = 5.5$–7.2 and $q_{95} = 3.7$–4.5. Here ν_e^*, ρ_{pol}^*, T_e, T_i, R/L_{n_e} and q_{95} are, respectively, the normalized effective electron collision frequency, the normalized ion poloidal Larmor radius, the electron and ion temperatures, the inverse ratio of density scale length, L_{n_e}, to the major radius, R, and the safety factor at the 95% flux surface.

(Some figures may appear in colour only in the online journal)

1. Introduction

Prediction and control of the toroidal rotation velocity (V_ϕ) profile are critical issues in ITER from the viewpoint of improving confinement [1–5], relating to the H-mode threshold power [6], achieving magnetohydrodynamic (MHD) stability [7–10] and managing impurities [11, 12]. Momentum transport has been experimentally studied in many tokamaks, as well as momentum sources and sinks, in order to understand the physical mechanisms determining the V_ϕ profile [13–24]. The theoretical understanding of the physics of momentum transport has also progressed [25–31]. Transient toroidal momentum transport was examined and non-diffusive terms were found using tangential neutral beam injection (NBI) in JT-60U and JFT-2M [13, 14]. Studies of the toroidal momentum diffusivity (χ_ϕ) and the pinch velocity (V_{pinch}) have been actively pursued in several tokamak devices using developed transient momentum transport analyses [15–24] since the importance of both the diffusive and pinch terms to the V_ϕ profile had been widely recognized [32]. For example, a large inward momentum pinch was observed during edge-localized mode free (ELM-free) H-mode discharges in Alcator C-Mod [15]. The parametric dependence of χ_ϕ and V_{pinch}, and the correlation between χ_ϕ and χ_i have been investigated in JT-60U L-mode plasmas, where χ_ϕ increases with increasing heating power and decreases with increasing plasma current [16, 17]. In JT-60U H-mode plasmas, an increase in χ_ϕ/χ_i with increasing ion temperature and a decrease with increasing electron density were observed at the radial positions of $r/a =$ 0.3, 0.4 and 0.6. The ratio $-V_{pinch}/\chi_\phi$ at $r/a =$ 0.4, 0.5 and 0.6 increases with increasing ion and electron temperatures or temperature gradients [18]. In JET, the magnitude and radial profile of χ_ϕ are similar to those of χ_i, and the inward momentum pinch velocity is found to be up to $20\,\mathrm{m\,s^{-1}}$ in an H-mode plasma [19]. NSTX reported a decrease in χ_ϕ with increasing toroidal magnetic field (B_T) and little dependence of χ_ϕ and the inward pinch velocity on the plasma current (I_p) [20, 21]. The existence of the inward momentum pinch was also confirmed in DIII-D H-mode plasmas [22]. To predict the momentum transport coefficients in ITER, these observations should first be organized and a common trend in tokamaks should be identified and confirmed over a wide range of plasma parameters.

The purpose of this study is to find common features of momentum transport coefficients, i.e. the toroidal momentum diffusivity and the pinch velocity, in machines. Different characteristics in machines are investigated by comparing the experimental conditions in order to identify which plasma parameters are important for the momentum transport coefficients. A unique feature of this study is that the characteristics of momentum transport coefficients and its parametric dependences are assessed over a wider range of dimensionless parameters that are related to transport than in previous studies. Data from multiple machines enable the identification of results, which cannot be observed in one machine due to the lack of its dynamic range. To make a progress in this study, a momentum database activity has been developed using previously published data in Alcator C-Mod, DIII-D, JET, JT-60U and NSTX. Observations in this paper will contribute to the development of scaling/modelling for momentum transport on future devices like ITER and DEMO.

This paper is arranged as follows: in section 2, the contents and status of the momentum database are introduced. Using the momentum database, the correlation between χ_ϕ and V_{pinch} in H-mode plasmas among the various tokamaks is studied in section 3. Section 4 studies the parametric dependences of the momentum transport coefficients (χ_ϕ/χ_i, RV_{pinch}/χ_ϕ and χ_ϕ) using dimensionless and dimensional plasma parameters. Here χ_ϕ/χ_i and RV_{pinch}/χ_ϕ are the Prandtl number and pinch number, respectively. After some discussions in section 5, a brief summary is given in section 6.

2. Momentum database

A database of momentum transport (IMDB1v0) on five tokamaks, Alcator C-Mod, DIII-D, JET, JT-60U and NSTX, has been constructed under a wide range of conditions to access the characteristics of momentum transport coefficients. The momentum database consists of the momentum diffusivity (χ_ϕ) and the pinch velocity (V_{pinch}), which are obtained through transient transport analyses, and main plasma and engineering parameters.

The toroidal momentum diffusivity and the pinch velocity are evaluated using the toroidal momentum balance equations,

$$\frac{\partial m_i n_i V_\phi}{\partial t} = -\nabla \cdot M + S, \tag{1}$$

$$M = -m_i \chi_\phi \frac{\partial n_i V_\phi}{\partial r} + m_i V_{pinch} n_i V_\phi, \tag{2}$$

where m_i, n_i V_ϕ, M and S are the ion mass, ion density, toroidal rotation velocity, toroidal momentum flux and the toroidal momentum source, respectively. The momentum flux consists of the diffusive and pinch terms with the residual stress term being ignored in this model. While the neglecting of residual stress (or, intrinsic torque) is a shortcoming of this work, it can be justified by restricting the analysis to cases where it is believed to be small (discussed later).

When the ion density profile is flat in the region, the toroidal momentum flux can be written as

$$M = -m_i n_i \chi_\phi \frac{\partial V_\phi}{\partial r} + m_i V_{pinch} n_i V_\phi. \tag{3}$$

The time-independent solutions of χ_ϕ and V_{pinch} are calculated from the perturbed component of equations (1) and (2) or (1) and (3). The treatment of density profile in the momentum balance equations is different in devices. Alcator C-Mod, DIII-D, JET and NSTX take the density outside of the gradient in the momentum balance equation (3). JT-60U treats the density inside of the gradient (equation (2)). The deuterium density is calculated from the quasi-neutrality condition knowing the effective plasma ion charge (Z_{eff}) while assuming that carbon is the main impurity and Z_{eff} is a radial constant. The difference ($\partial n_i V_\phi/\partial r$ or $n_i \partial V_\phi/\partial r$) does not make a difference in χ_ϕ; however, the difference can vary V_{pinch} by 1.4–$13\,\mathrm{m\,s^{-1}}$ (discussed in the appendix).

In Alcator C-Mod, χ_ϕ and V_{pinch} are evaluated in terms of the evolution of the toroidal rotation velocity profile at L–H and H–L transitions using a simple source-free momentum transport model [15]. The source of the momentum due to the L–H transition was located in the plasma edge, and

Table 1. Overview of the range of some plasma and engineering parameters in the momentum database. The ranges of the plasma current (I_p), the toroidal magnetic field (B_T), the line-averaged electron density ($\bar{n}_e$) and the absorbed power (P_{ABS}) with actuators are described. R is the major radius. CW and CCW mean the clockwise direction and the counter-clockwise direction from the top, respectively. The database consists of L-mode and H-mode plasmas.

Device	Normalized radius	R (m)	I_p (MA)	B_T (T)	q_{95}	$\bar{n}_e$ (10^{19} m^{-3})	P_{ABS} (MW)
Alcator C-Mod	0, 0.3, 0.6	0.68–0.69	0.79–0.8 (CW)	4.6–5.5 (CW)	4.3–5.2	13.1–26.8	0.47–2.89 (OH, ICRF)
DIII-D	0.5, 0.55, 0.6, 0.65, 0.7, 0.75, 0.8	1.72–1.79	0.6–1 (CCW)	1.3–1.8 (CW)	4.1–5.8	2.7–3.8	1.6–4.7 (NB)
JET	0.3, 0.4, 0.5, 0.6, 0.7	2.93–3.02	1.5–2.5 (CCW)	3 (CCW)	4.0–7.1	5.1–8.3	7–22 (NB, ICRF)
JT-60U	0.3, 0.4, 0.5, 0.6	3.35–3.52	0.9–1.8 (CW)	2.8–4.0 (CW)	3.7–8.2	1.2–2.5	2.1–10.7 (NB)
NSTX	0, 0.1, 0.2, 0.5, 0.6, 0.7, 0.8	0.99–1.05	0.7–1.1 (CCW)	0.34–0.54 (CW)	6.7–14.1	4.2–7.1	3.9–5.9 (NB)

the boundary conditions of an edge rotation changed from 0 to V_0 at the L–H transition. In DIII-D, χ_ϕ and V_{pinch} are inferred from momentum balance equations (1) and (3) in TRANSP [33] during the rotation relaxation following the NB blip perturbations [22]. The torque profile deposited by the NB blip is calculated using the NUBEAM [34, 35] package within TRANSP. In the perturbation experiments, the effective torque associated with intrinsic rotation was not significantly changed and the non-resonant magnetic field (NRMF) torque [36, 37] modulation was at least a factor of 4–5 smaller than that from the torque from NB blips. In JET, χ_ϕ and V_{pinch} are determined from time-dependent transport modelling through tangential NBI modulation experiments [19, 23]. The steady-state value of toroidal rotation is also simulated as a third constraint, in addition to the amplitude and phase. The NBI-induced torque, which consists of collisional and $j \times B$ torques [38–40], is calculated with the NUBEAM code inside the TRANSP code. H-mode plasmas with type-III ELMs at low collisionality and high q_{95} to avoid sawteeth were chosen to perform the cleanest possible rotation modulation. In NSTX, perturbation experiments, which yielded χ_ϕ and V_{pinch}, were performed using NB pulses (200 ms, $P_{NB} = 4$ MW) and/or non-resonant $n = 3$ magnetic field pulses (40–50 ms) [20, 21]. In JT-60U, the perturbation technique with perpendicular NBs, which enhances the rotation in the counter-current direction by the fast ion losses due to the toroidal field ripple in the peripheral region, is used [16]. The momentum balance equation is solved using a cylindrical model for toroidal momentum with flux surface averaged parameters assuming the source is negligible [16]. Details of the experiments and analyses for each machine are given in the appendix. The residual stress term can be ignored in this study for the following reasons. The residual stress is predicted to be potentially important in regions of steep pressure gradient [41] in the vicinity of either internal or edge transport barriers. None of the plasmas used in this study exhibited internal transport barriers, and the momentum transport coefficients are evaluated inside edge transport barriers. In Alcator C-Mod, the intrinsic torque was localized at the pedestal region and was found to have little effect on the source-free core momentum transport [42]. In DIII-D and JT-60U, the intrinsic rotation was not significantly changed during perturbation experiments, as the pressure gradient was not perturbed during these experiments. In steady-state scenarios with NBI in JET, the intrinsic torque was maximum 20% of the beam torque. Therefore, the estimated effect of the intrinsic torque on χ_ϕ/χ_i and RV_{pinch}/χ_ϕ are within the error bar (typically 30%).

An overview of the range of some plasma and engineering parameters is summarized in table 1. A total of 68 discharges, 254 data points, including L- and H-mode plasmas are collected in the momentum database. The momentum database contains 18 global parameters and 31 local dimensional parameters, which can describe the general plasma conditions and dimensionless parameters. The data of six shots and three radial positions of $r/a = 0$, 0.3 and 0.6 (a total of 18 data) are supplied by Alcator C-Mod. There are three H-mode plasmas and three L-mode plasmas. The plasma current (I_p) and the toroidal magnetic field (B_T) remain almost constant and both I_p and B_T. The line-averaged density ($\bar{n}_e$) and the absorbed power (P_{ABS}) are scanned from 13.1×10^{19} to 26.8×10^{19} m^{-3} and from 0.47 to 2.89 MW by varying the ICRF power, respectively. From DIII-D, the data every 0.05 of the normalized minor radius (r/a) in the outer region of the plasma ($r/a = 0.5$–0.8) are supplied. There are two H-mode plasmas and three L-mode plasmas. The absorbed power varies from 1.6 to 4.7 MW (a factor of 3) by varying the NB power. The energy confinement time, normalized to the ITER89-P scaling [43], in these discharges is lower ($H_{89} < 2$) than that in typical DIII-D H-mode plasmas due to the unusual startup conditions. In JET, data of type-III ELMy H-mode discharges (eight discharges) are selected to avoid the influence of ELMs on transport analysis. No strong MHD activity, except sawteeth, was observed in any of the discharges. Data of highest heating plasma current and heating power are supplied to the momentum database from JET; $I_p = 2.5$ MA and $P_{ABS} = 22$ MW with NB and ICRF heating. In NSTX, most of the data are taken in the outer region of H-mode plasmas ($r/a = 0.5$–0.8, 26 discharges). Both I_p and B_T are scanned by a factor of ≈ 1.6. The triangularity at the 95% flux surface (δ_{95}) is scanned from 0.64 to 0.86 at constant elongation at the 95% flux surface of $\kappa_{95} \approx 2.4$. In JT-60U, data from $r/a \approx 0.3$ to 0.6 were measured and a total of 23 shots (15 H-mode plasmas and 9 L-mode plasmas), 92 data points, are supplied. The plasma current, magnetic field and density are scanned by a factor of about two. The heating power varies from 2.1 to 10.7 (a factor of ≈ 5) by varying the NB power. No strong MHD activity, except sawtooth, appears even in high-power regimes.

Figure 1 shows the plasma regimes of the present database. Different symbols are for different machines. Open symbols mean the data are from L-mode plasmas and closed symbols indicate the data are from H-mode plasmas. The data cover a wide region of $I_p = 0.7$–2.5 MA, $B_T = 0.4$–5.5 T, $\bar{n}_e = 1.2 \times 10^{19}$–$2.6 \times 10^{20}$ m^{-3} and $P_{ABS} = 0.5$–22 MW. In JET
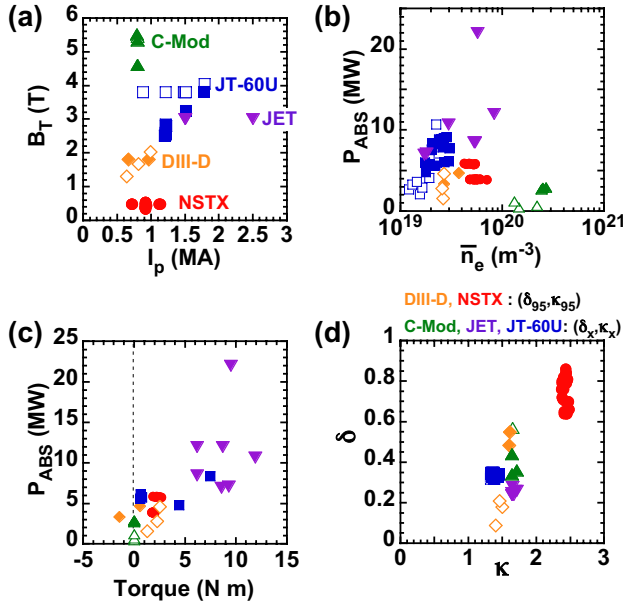
Figure 1. Plasma regimes of the momentum database comprising five machines: Alcator C-Mod (green triangles), DIII-D (orange diamonds), JET (purple inverted triangles), NSTX (red circles) and JT-60U (blue squares). Open symbols mean the data of L-mode plasmas and closed symbols indicate the data of H-mode plasmas. (*a*) The toroidal magnetic field (B_T) versus the plasma current (I_p), (*b*) the absorbed power (P_{ABS}) versus the line-averaged electron density ($\bar{n}_e$), (*c*) the absorbed power versus torque and (*d*) triangularity (δ) versus elongation (κ).

plasmas and some of the plasmas in JT-60U, a comparatively large torque of $=5$–11 Nm was injected with the tangential beams pointed in the same direction as that of the plasma current (CO-NBs). Such a variety of experimental conditions enables the assessment of a parametric dependence over a wide range of dimensional and dimensionless parameters.

## 3. Correlations between χ_ϕ and χ_i, χ_ϕ and V_{pinch}

The momentum database is now used to study the properties of momentum transport. For this study, only H-mode plasmas without strong MHD activity are selected. Figure 2 shows examples of the radial profiles of the momentum diffusivity (χ_ϕ) and the pinch velocity (V_{pinch}) in DIII-D, JET, NSTX and JT-60U. The negative sign of V_{pinch} denotes the inward pinch. In DIII-D, shown in figure 2(*a*), an NB power of 5.4 MW and an ECRF power of 2.3 MW were injected in a steady-state H-mode plasma ($I_p = 1.0$ MA, $B_T = 1.8$ T) [22]. During the NB blip perturbation, the normalized beta (β_N) remained constant. In JET shown in figure 2(*b*), an NB power of 9.3 MW was injected in a type-III ELMy H-mode plasma ($I_p = 1.5$ MA, $B_T = 3.0$ T) [19]. In NSTX shown in figure 2(*c*), an NB power of 2 MW was injected in an H-mode plasma ($I_p = 0.9$ MA, $B_T = 0.45$ T) [20, 21]. In JT-60U shown in figure 2(*d*), an NB power of 9.8 MW was injected in a type-I ELMy H-mode plasma ($I_p = 1.2$ MA, $B_T = 2.6$ T) [18]. The inversion radius of the sawtooth oscillations was inside of $r/a \approx 0.25$, and the ELM affected area was outside of $r/a \approx 0.7$. The momentum transport coefficients are not evaluated in the outer region $r/a > 0.65$ because the ripple
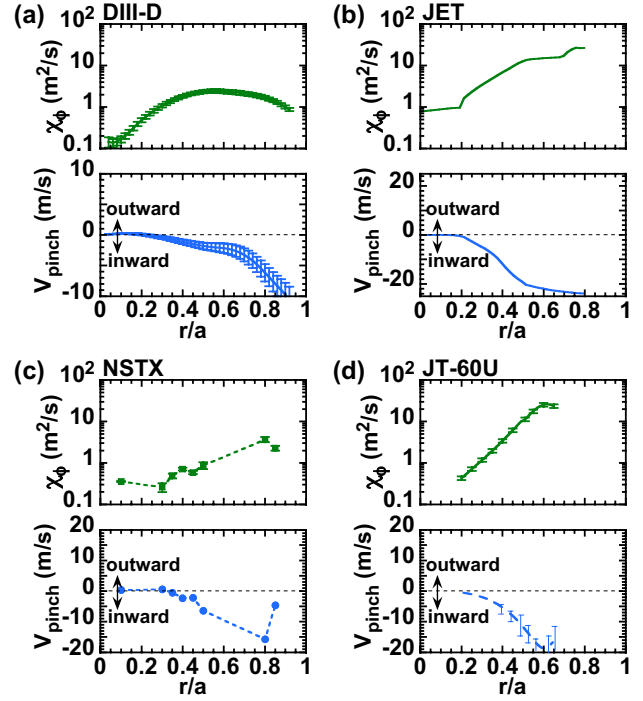
Figure 2. Radial profiles of the momentum diffusivity (χ_ϕ) and the pinch velocity (V_{pinch}) in plasmas of (*a*) DIII-D, (*b*) JET, (*c*) NSTX and (*d*) JT-60U. The negative sign of V_{pinch} denotes the inward pinch.

loss of fast ions, which induces a $j \times B$ torque, is localized in the peripheral region $r/a > 0.7$. Comparing the profiles from four machines (figure 2), a similarity of χ_ϕ profile is observed; χ_ϕ becomes larger in the outer region of the plasma in all devices. Such profiles are observed in other plasmas collected in the database; χ_ϕ is larger in the outer region of the plasma on JET and JT-60U. In NSTX, although the measurement range is small $r/a = 0.6$–0.85, the majority of the discharges (90% of the discharges) exhibit larger χ_ϕ in the outer region. Similarity of profiles is also observed in V_{pinch}; $-V_{pinch}$ increases in radius and an inward pinch is mostly observed in all five machines and in most of the discharges (85% of the discharges).

The correlation between χ_ϕ and χ_i is compared among the five tokamaks, and the results are shown in figure 3(*a*). Different symbols again denote the different machines at $r/a = 0.6$. This radius is used since all devices have results at this location, and it avoids the influence of sawteeth near the plasma centre and ELMs in the edge region. While an overall correlation between χ_ϕ and χ_i can be observed using the data from all five machines, the relations within the dataset from each individual device are more subtle. The momentum diffusivity, χ_ϕ, is larger than or equal to χ_i in JET and JT-60U. On the other hand, χ_ϕ is smaller than or equal to χ_i in NSTX, DIII-D and Alcator C-Mod. The variations of χ_ϕ/χ_i will be discussed in section 4. NSTX data exhibit the relation between χ_ϕ and χ_i over a wide range of χ_i (about one order of magnitude). The variation of χ_i is associated with a change in Z_{eff}. A variation of χ_ϕ at constant χ_i can be seen in JET and JT-60U. In JT-60U, an increase in χ_ϕ is observed with increasing T_i through a heating power scan, while χ_i remains almost constant [18]. The momentum diffusivity in JET tends to increase with T_e at constant I_p (this trend will be discussed
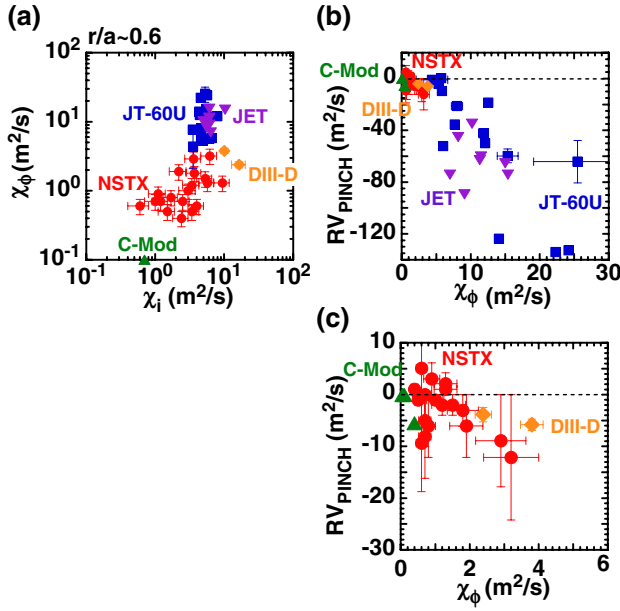
Figure 3. (*a*) Correlation between χ_ϕ and the heat diffusivity (χ_i) in five machines. (*b*) Correlation between χ_ϕ and V_{pinch} at $r/a = 0.6$. (*c*) An enlarged view of (*b*) for Alcator C-Mod, DIII-D and NSTX.

in section 4). Thus, χ_ϕ/χ_i is not constant but can vary with varying plasma parameters.

The correlation between χ_ϕ and RV_{pinch} at $r/a = 0.6$ is also compared in five tokamaks, as shown in figure 3(*b*). Figure 3(*c*) is an enlarged view of figure 3(*b*) for $0 \leqslant \chi_\phi \leqslant 6\,\text{m}^2\,\text{s}^{-1}$ to show the Alcator C-Mod, DIII-D and NSTX data. A general trend is observed in all tokamaks; $-RV_{pinch}$ increases with increasing χ_ϕ over a wide range of the momentum transport coefficients, covering roughly two orders of magnitude. It should be mentioned that this trend ($-V_{pinch}$ increases with increasing χ_ϕ) is still observed even though the value of V_{pinch} can vary in JT-60U by 1.4–$13\,\text{m}\,\text{s}^{-1}$ due to the treatment of density in the momentum balance equation (discussed in the appendix). The strong correlation between χ_ϕ and RV_{pinch} could have an impact on the toroidal rotation prediction in future devices.

Comparisons of χ_ϕ/χ_i in machines are shown over the whole radius in figure 4. The difference in colour corresponds to the different radial positions and the solid lines show $\chi_\phi = \chi_i$. The dashed lines show a least-squares fit for each radius. In these fits, a linear model passing through the origin ($\chi_\phi = (\alpha \pm \varepsilon)\chi_i$) is applied. Here χ_ϕ is the dependent variable and χ_i is the independent variable. The result of the fit (the coefficient, α), the uncertainty of the fitted parameter (the standard error, ε) and the goodness of fit (the linear correlation coefficient in the least-squares fitting, R) are summarized in table 2. In JET, shown in figure 4(*a*), χ_ϕ is equal to or slightly higher than χ_i over the whole radius. Figure 4(*a*) exhibits that the correlation between χ_ϕ and χ_i exists at each radial location and the ratio χ_ϕ/χ_i becomes larger in the outer region. Similarly, the JT-60U data show that χ_ϕ is mostly greater than or equal to χ_i and the ratio χ_ϕ/χ_i becomes larger in the outer region, as shown in figure 4(*b*). The radial profile of χ_ϕ/χ_i will be discussed in the next paragraph. Although χ_ϕ is roughly correlated with χ_i over the radius, the goodness of fit in JT-60U is very low at a radial
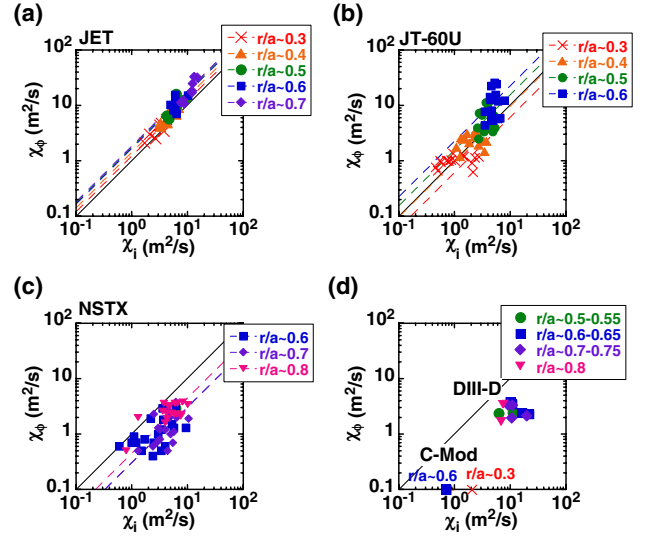

Figure 4. Comparisons of χ_ϕ/χ_i in machines: (*a*) JET, (*b*) JT-60U, (*c*) NSTX and (*d*) DIII-D and Alcator C-Mod. The difference in colour corresponds to the different radial positions, and the solid lines show $\chi_\phi = \chi_i$ and the dashed lines mean the least-squares fit for each radius. The results of the fit for each dataset are shown in table 2.

Table 2. Result of the fit (the coefficient, α), the standard error (ε), the linear correlation coefficient in the least-squares fitting (R) of a linear model ($\chi_\phi = (\alpha \pm \varepsilon)\chi_i$), and the number of data for JET, JT-60U and NSTX plasmas.

Device	α (coefficient)	ε (standard error)	R (correlation coefficient)	Number of data
JET				
$r/a = 0.3$	1.212	0.071	0.855	8
$r/a = 0.4$	1.415	0.102	0.847	8
$r/a = 0.5$	1.752	0.168	0.593	8
$r/a = 0.6$	1.660	0.149	0.529	8
$r/a = 0.7$	1.835	0.162	0.891	8
JT-60U				
$r/a = 0.3$	0.611	0.094	0.206	15
$r/a = 0.4$	0.965	0.121	0.035	15
$r/a = 0.5$	0.965	0.207	0.034	15
$r/a = 0.6$	2.247	0.355	0.112	15
NSTX				
$r/a = 0.6$	0.304	0.047	0.459	19
$r/a = 0.7$	0.302	0.042	0.404	19
$r/a = 0.8$	0.447	0.039	0.540	19

position. This means the ratio χ_ϕ/χ_i can vary with varying plasma parameters. For example, there are some data points, which show $\chi_\phi/\chi_i < 1$. These correspond to discharges where a large amount of D_2 gas of ≈ 10–$30\,\text{Pa}\,\text{m}^3\,\text{s}^{-1}$ is puffed at a constant NBI power in the plasmas, and then n_e increases and T_i decreases simultaneously. JT-60U reported that χ_ϕ decreases with increasing n_e and/or decreasing T_i while χ_i remains constant [18]. In contrast, in NSTX, DIII-D and Alcator C-Mod, χ_ϕ is smaller than χ_i, as shown in figures 4(*c*) and (*d*). In NSTX, χ_ϕ/χ_i is about 0.3–0.4 in the region of $r/a = 0.6$–0.8. In DIII-D, χ_ϕ/χ_i is about 0.1–0.2 in the region of $r/a = 0.5$–0.8. In Alcator C-Mod, χ_ϕ/χ_i is about 0.1 over the whole radius. Note that χ_i in NSTX is significantly lower than that in JET or JT-60U. Part of this may be due to the ion thermal transport in NSTX being close to neoclassical [21],
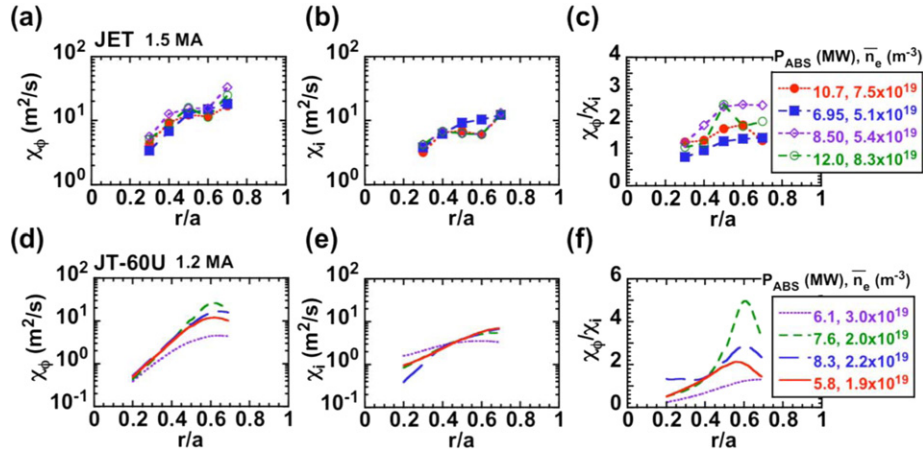
Figure 5. Radial profiles of χ_ϕ, χ_i and χ_ϕ/χ_i in JET (*a*)–(*c*), and in JT-60U (*d*)–(*f*). The absorbed power and electron density are scanned at a constant plasma current in each machine.

while it is more anomalous in the other two devices. The difference in operating regimes for $\chi_\phi/\chi_i \geqslant 1$ and $\chi_\phi/\chi_i < 1$ will be discussed in section 4.

Another property of χ_ϕ/χ_i can be seen in figure 5. Figures 5(*a*)–(*c*) show the radial profiles of χ_ϕ, χ_i and χ_ϕ/χ_i for four JET discharges. Figures 5(*d*)–(*f*) show the same profiles for four JT-60U discharges. In both machines, the absorbed power and electron density are scanned at constant plasma current and toroidal magnetic field of $I_p/B_T = 1.5\,\text{MA}/3\,\text{T}$ (JET) and $I_p/B_T = 1.2\,\text{MA}/2.6\,\text{T}$ (JT-60U). Although χ_ϕ varies by one order of magnitude radially in both machines, it can be seen that χ_ϕ/χ_i varies only by a factor of ≈ 1.5–5. Moreover, the ratio χ_ϕ/χ_i becomes larger in the outer region in both machines. In JET, even in the relatively flat χ_ϕ/χ_i profile case ($P_{\text{ABS}} = 6.95\,\text{MW}$, $\bar{n}_e = 5.1 \times 10^{19}\,\text{m}^{-3}$), the value of χ_ϕ/χ_i is about 1.5 times larger at the outer position ($r/a \approx 0.6$) than at the inner position ($r/a \approx 0.3$). The error bar of χ_ϕ/χ_i is estimated to be about 30% in JET, which is much smaller than the variation of χ_ϕ/χ_i. In JT-60U, the error bar of χ_ϕ/χ_i is also about 30% for the most flat χ_ϕ/χ_i profile case ($P_{\text{ABS}} = 6.1\,\text{MW}$, $\bar{n}_e = 3.0 \times 10^{19}\,\text{m}^{-3}$), which is also much smaller than the variation of χ_ϕ/χ_i. Such a variation of χ_ϕ/χ_i in the radial direction is observed in most of the discharges in JET and JT-60U ($\approx 90\%$ of the discharges). These results (χ_ϕ correlates with χ_i, χ_ϕ/χ_i varies only by a factor of ≈ 1.5–5 radially and χ_ϕ/χ_i becomes larger in the outer region) provide important information for identifying the underlying physics controlling both heat and momentum transport, and thus may form part of the basis of prediction to ITER.

Comparisons of $RV_{\text{pinch}}/\chi_\phi$ in each machine are shown in figure 6. The dashed lines show a least-squares fit for each radius. In these fits, a linear model passing through the origin is applied ($RV_{\text{pinch}} = (\beta \pm \varepsilon)\chi_\phi$) and the coefficient, β is the local plasma parameter. Here RV_{pinch} is the dependent variable and χ_ϕ is the independent variable. The result of the fit, the uncertainty of the fitted parameter (the standard error, ε) and the goodness of fit (R) are summarized in table 3. In the previous discussion of figure 3(*b*), a general trend in all tokamaks was observed; $-RV_{\text{pinch}}$ increases with χ_ϕ at $r/a = 0.6$. Such a correlation is measured at other radial
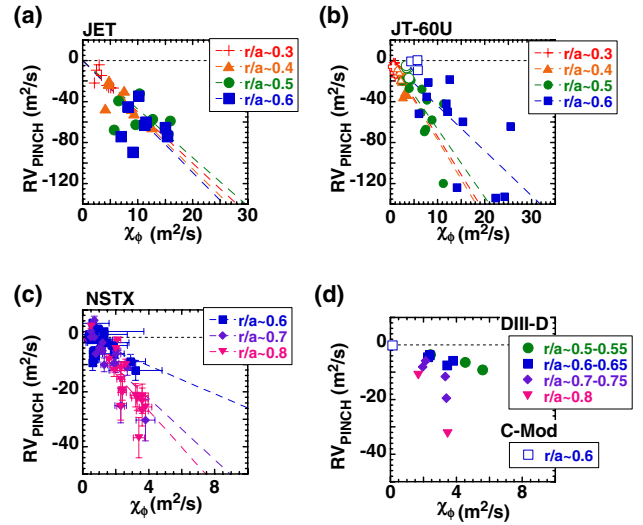
Figure 6. Comparisons of $RV_{\text{pinch}}/\chi_\phi$ in each machine: (*a*) JET, (*b*) JT-60U, (*c*) NSTX and (*d*) DIII-D and Alcator C-Mod. The difference in colour corresponds to the different radial positions. The dashed lines show the least-squares fit for each radius. The results of the fit for each dataset are shown in table 3. Discharges indicated by open symbols in (*b*) correspond to those in figure 7(*d*).

positions in each machine. In JET, $-RV_{\text{pinch}}$ increases with increasing χ_ϕ in a similar way at all radii, and $RV_{\text{pinch}}/\chi_\phi$ is about -5 in the region $r/a = 0.3$–0.6. In JT-60U, $RV_{\text{pinch}}/\chi_\phi$ is about -7 in the inner region of the plasma ($r/a < 0.5$) and tends to be smaller in the outer region. A subset of JT-60U discharges is observed to have very low V_{pinch} or $RV_{\text{pinch}}/\chi_\phi$. These discharges are identified as ones where a large amount of D_2 gas was injected and the density profile became somewhat flatter. They are identified by open symbols in figure 6(*b*). In NSTX and DIII-D, RV_{pinch} and χ_ϕ are evaluated mainly in the outer region of the plasma (from $r/a = 0.5$ or 0.6 to 0.8). The ratio $RV_{\text{pinch}}/\chi_\phi$ tends to be larger at the peripheral regions ($r/a \approx 0.7$–0.8) in both machines. In DIII-D, the ratio $RV_{\text{pinch}}/\chi_\phi$ at $r/a = 0.5$–0.6 is about -2, which is small compared with that in other tokamaks. Although the ratio $RV_{\text{pinch}}/\chi_\phi$ can vary by varying the plasma and experimental conditions, a robust correlation

Table 3. Result of the fit (the coefficient, β), the standard error (ε), the linear correlation coefficient in the least-squares fitting (R) of a linear model ($RV_{pinch} = (\beta \pm \varepsilon)\chi_\phi$), and the number of data for JET, JT-60U and NSTX plasmas.

| Device	β (coefficient)	ε (standard error)	R (correlation coefficient)	Number of data
JET				
$r/a = 0.3$	-4.997	0.558	0.693	8
$r/a = 0.4$	-5.274	0.478	0.768	8
$r/a = 0.5$	-4.723	0.584	0.315	8
$r/a = 0.6$	-5.447	0.716	0.097	8
JT-60U				
$r/a = 0.3$	-7.414	0.878	0.552	15
$r/a = 0.4$	-7.697	0.627	0.738	15
$r/a = 0.5$	-6.657	0.760	0.797	15
$r/a = 0.6$	-4.392	0.547	0.789	15
NSTX				
$r/a = 0.6$	-2.585	0.648	0.539	19
$r/a = 0.7$	-5.589	0.806	0.868	19
$r/a = 0.8$	-6.703	0.562	0.817	19

between χ_ϕ and RV_{pinch} is found by comparing the data in machines and in radial positions. The correlation coefficients of the $RV_{pinch} = \beta\chi_\phi$ model are mostly above 0.7 (table 3).

4. Parameter dependences of momentum transport coefficients
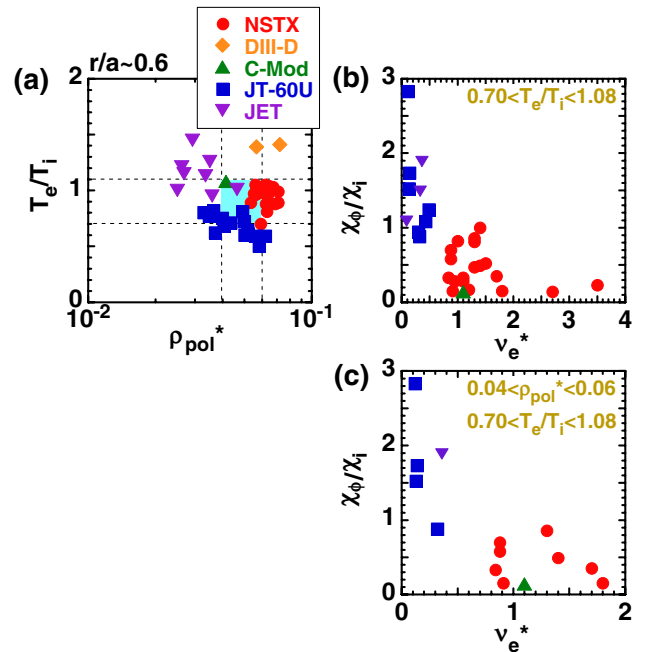
4.1. Parameter dependence of χ_ϕ/χ_i

In section 3, a general trend for χ_ϕ to increase with χ_i over a wide range of χ_ϕ was found. However, variation of χ_ϕ/χ_i was observed between machines, as shown in figures 3 and 4; χ_ϕ is greater than χ_i in JET and JT-60U; χ_ϕ is smaller than χ_i in Alcator C-Mod, DII-D and NSTX. In this section, the operating regimes in the cases with $\chi_\phi/\chi_i \geqslant 1$ and $\chi_\phi/\chi_i < 1$ are characterized, by both dimensionless and dimensional parameters, and then the parametric dependences of χ_ϕ/χ_i and χ_ϕ are discussed using the characterized dimensionless and dimensional parameters, respectively. For the same reasons as discussed in the previous section, the data at $r/a = 0.6$ are used for these analyses.

The range of plasma parameters at $r/a = 0.6$ is summarized in figure 7. Here ρ_{pol}^*, ν_e^* and R/L_{n_e} are, respectively, the normalized ion poloidal Larmor radius, the normalized effective electron collision frequency and the inverse ratio of density scale length, L_{n_e}, to the major radius, R. In the calculation of the density scale length, data are averaged over $r/a = 0.4$–0.8 in JET. The density scale length is taken locally, with no spatial averaging, in DIII-D, JT-60U and NSTX. For all devices, the density profiles were fitted by splines. The operating regime in ITER is indicated in figure 7(c). Experiments in NSTX and Alcator C-Mod, where χ_ϕ is smaller than χ_i, were performed in relatively high density and low temperature regimes, as shown in figure 7(a), or, equivalently, in relatively higher ν_e^* regimes, as shown in figure 7(c). In DIII-D, experiments were in higher ρ_{pol}^* regimes since the ion temperature was similar to that in JET but the poloidal magnetic field was lower. The operating regime of JT-60U, where a relatively higher $\chi_\phi/\chi_i \approx 2$–5 is observed, is characterized by high T_i, low T_e/T_i, as shown in figures 7(b) and (d).
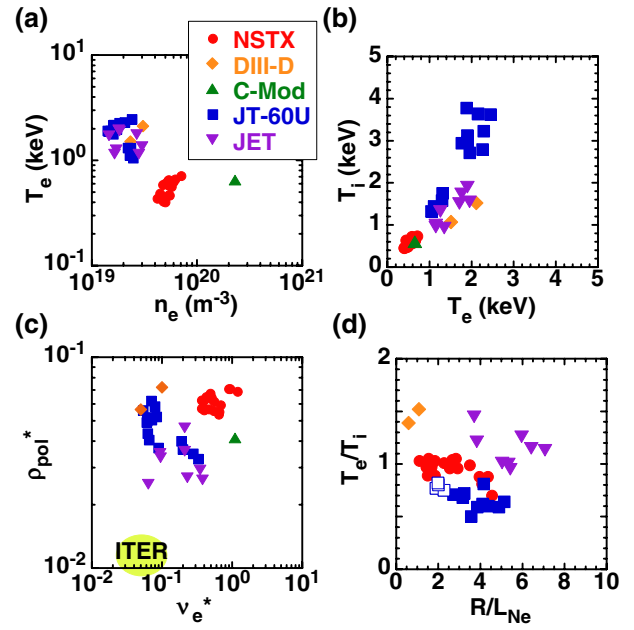
Figure 7. Range of some plasma parameters at $r/a = 0.6$ in the five machines: Alcator C-Mod (green triangles), DIII-D (orange diamonds), JET (purple inverted triangles), NSTX (red circles) and JT-60U (blue squares). (a) The electron temperature (T_e) versus the electron density (n_e), (b) the ion temperature (T_i) versus the electron temperature (T_e), (c) the normalized ion poloidal Larmor radius (ρ_{pol}^*) versus the normalized effective electron collision frequency (ν_e^*) and (d) the ratio of electron and ion temperatures (T_e/T_i) versus the inverse ratio of density scale length, L_{n_e} to the major radius, R. The ITER regime is also shown by hatched areas.


Figure 8. (a) Parameter regimes for ν_e^* dependence. (b) Relation between χ_ϕ/χ_i and ν_e^* at fixed T_e/T_i and (c) the relation at fixed T_e/T_i and ρ_{pol}^*.

The trends shown in figure 7 provide a framework for studying the dependence of χ_ϕ/χ_i on dimensionless parameters that may reflect the plasma's transport properties. The dependence of χ_ϕ/χ_i on ν_e^* at fixed T_e/T_i and ρ_{pol}^* in H-mode

plasmas is shown in figure 8. Here again, different symbols denote the different machines. Ranges of T_e/T_i from 0.70 to 1.08 and ρ^*_{pol} from 0.04 to 0.06 are selected (hatched region in figure 8(*a*)). Both ranges ($T_e/T_i = 0.70$–1.08 and $\rho^*_{pol} = 0.04$–0.06) are $\pm 20\%$ of the average of $T_e/T_i = 0.9$ and $\rho^*_{pol} = 0.05$, respectively. The ratio χ_ϕ/χ_i is plotted as a function of ν^*_e using the selected data in figures 8(*b*) and (*c*). Figure 8(*b*) shows the relation between χ_ϕ/χ_i and ν^*_e at fixed T_e/T_i, and figure 8(*c*) illustrates the relation at fixed T_e/T_i and ρ^*_{pol}. Although it is difficult to state the dependence in each machine dataset due to the small ν^*_e range, overall χ_ϕ/χ_i tends to be smaller in high ν^*_e when taking data points from all machines. The effect of collisionality on χ_ϕ/χ_i was calculated with quasilinear gyro-kinetic simulations in the presence of the ion temperature gradient (ITG) mode [31]. The simulations showed that χ_ϕ/χ_i decreased with increasing collisionality. This trend is qualitatively consistent with the experimental observation in figures 8(*b*) and (*c*). On the other hand, the dependence between χ_ϕ/χ_i on collisionality in the simulations remained weak in the low collisionality regimes and the reduction in χ_ϕ/χ_i is not large compared with the experimental observation. As mentioned previously, however, the NSTX ion thermal diffusivity is close to the neoclassical value, so the relation with ITG is not as clear as it may seem. It was impossible to investigate the ρ^*_{pol} dependence because of the very small dataset and the narrow range in ρ^*_{pol} with fixed T_e/T_i and ν^*_e. A T_e/T_i dependence cannot be assessed for the same reason. To investigate further the dependence of χ_ϕ/χ_i on ν^*_e, χ_ϕ and χ_i are plotted as functions of n_e and T_e in figure 9 (the same dataset in figure 7). An increase in χ_ϕ is observed with decreasing n_e and/or increasing T_e. The data cover a wide range of density $n_e = 1.4 \times 10^{19}$–$2.3 \times 10^{20}\,\mathrm{m}^{-3}$ (more than a factor of 16) and temperature $T_e = 0.4$–$2.45\,\mathrm{keV}$ (a factor of >6). The decrease in χ_ϕ with increasing n_e is observed on each machine. In contrast, χ_i shows a weak dependence on n_e and no dependence on T_e. Thus, the dependence of χ_ϕ/χ_i on $\nu^*_e \propto n_e/T_e^2$ is observed.

4.2. Parameter dependences of RV_{pinch}/χ_ϕ

In section 3, most of the machines show a robust correlation between χ_ϕ and RV_{pinch}. However, RV_{pinch}/χ_ϕ can vary, to some degree, with varying plasma and experimental conditions. Here, the operating regimes for large and small RV_{pinch}/χ_ϕ at $r/a = 0.6$ are investigated and then a parametric dependence of RV_{pinch}/χ_ϕ is discussed, considering the operating regimes. There is a common condition for small RV_{pinch}/χ_ϕ in DIII-D and JT-60U. The DIII-D operating regime can be characterized by a long density scale length (i.e. small R/L_{n_e} or small density gradient), as shown in figure 7(*d*). In JT-60U, a small V_{pinch} (or RV_{pinch}/χ_ϕ) is observed with a relatively flat density profile. Discharges indicated by open symbols in figure 7(*d*) correspond to those with open symbols in figure 6(*b*). Effects of various parameters on RV_{pinch}/χ_ϕ were predicted by gyro-kinetic calculations based on the ITG mode [27]. An increase in pinch velocity with increasing density gradient is predicted by the simulations. The gyro-kinetic calculation also predicts the effect of safety factor on RV_{pinch}/χ_ϕ [27]. Based on the theoretical predictions and experimental observations, the dependence of RV_{pinch}/χ_ϕ on
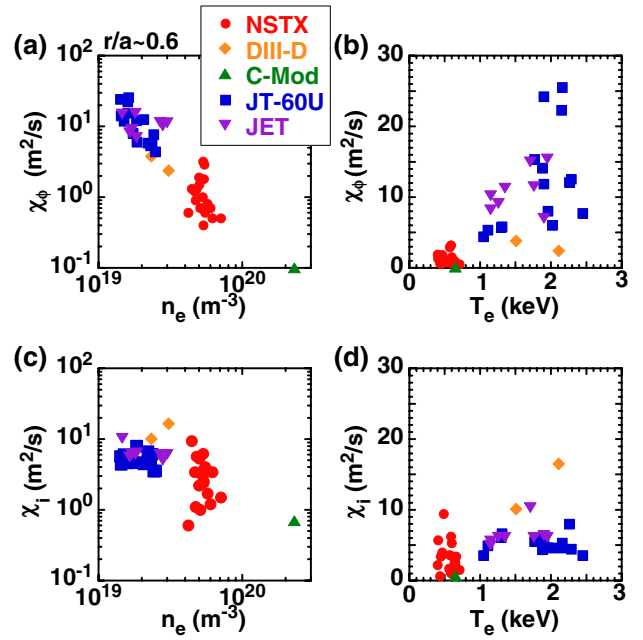
Figure 9. Relation between (*a*) χ_ϕ and n_e, (*b*) χ_ϕ and T_e; the relation between (*c*) χ_i and n_e, (*d*) χ_i and T_e at $r/a = 0.6$.
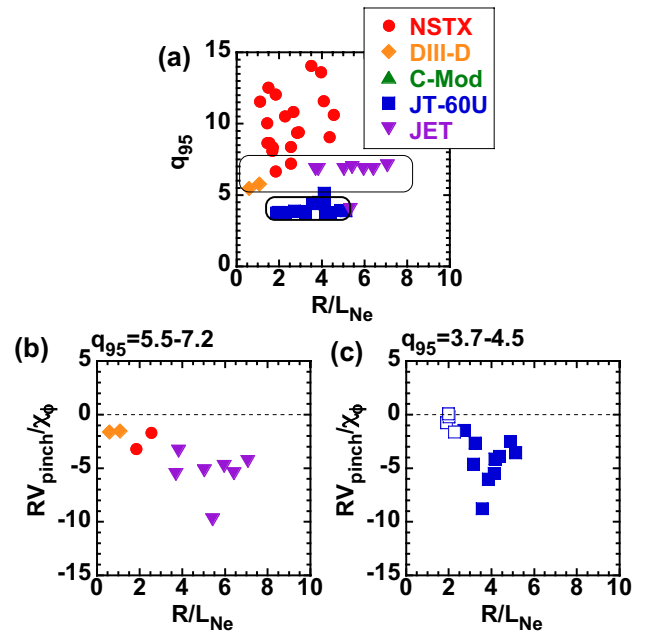
Figure 10. (*a*) Operating regimes for q_{95} and R/L_{n_e}. (*b*) Relation between RV_{pinch}/χ_ϕ and R/L_{n_e} at fixed $q_{95} = 5.5$–7.2. (*c*) Relation between RV_{pinch}/χ_ϕ and R/L_{n_e} at fixed $q_{95} = 3.7$–4.5. Discharges indicated by open symbols in (*c*) correspond to those in figures 6(*b*) and 7(*d*).

R/L_{n_e} at a fixed q_{95} is investigated here. Figure 10(*a*) shows the operating regimes for q_{95} and R/L_{n_e} in the momentum database. The dependence is investigated using two data subsets as denoted by thin and bold lines. The first is the dataset at $q_{95} = 5.5$–7.2 ($\pm 13\%$ of $q_{95} = 6.4$), which consists of data from DIII-D, JET and NSTX. The second is the dataset at $q_{95} = 3.7$–4.5 ($\pm 10\%$ of $q_{95} = 4.1$), which consists of data from JT-60U only. These datasets are selected to keep a wide range of

R/L_{n_e} at a fixed q_{95}. Moreover, each dataset consists of the pinch number (RV_{pinch}/χ_ϕ) evaluated by the same treatment of the density profile in the momentum balance equation, i.e. the datasets for DIII-D, JET and NSTX use equation (3) for V_{pinch} and the dataset for JT-60U uses equation (2). The dependences of RV_{pinch}/χ_ϕ on R/L_{n_e} at a fixed q_{95} are shown in figures 10(*b*) and (*c*). The two datasets, from four machines, all have the pinch number ($-RV_{pinch}/\chi_\phi$) increasing with increasing R/L_{n_e} in both q_{95} regimes. The observed dependence is qualitatively consistent with the theoretical prediction from the gyro-kinetic calculations [27]. This would be consistent with the momentum transport being dominated by ITG modes. This observation is also consistent with the result in JET, where a strong R/L_{n_e} dependence of the momentum pinch was clearly observed in a systematic scan of R/L_{n_e} [24].

5. Discussion: issues for scaling

Development of a scaling of χ_ϕ/χ_i is one of the important issues for future machines such as ITER and DEMO. In order to develop a reliable scaling of χ_ϕ/χ_i, it is necessary to investigate parameter dependences for all dimensionless parameters related to transport. In this paper, although the ν_e^* dependence is investigated at fixed T_e/T_i and ρ_{pol}^*, the ρ_{pol}^* and T_e/T_i dependence cannot be obtained due to the very small dataset and the narrow range in ρ_{pol}^* and T_e/T_i. In addition, there are few overlapping operating regimes between machines in the present database. Data in overlapping operating regimes will give more reliable analysis. Thus, more data points are required to produce a database sufficiently conditioned for a scaling. In addition to the experimental approach, a theoretical approach will be needed to explain the experimental results and to understand the momentum transport process. In this study, the momentum transport was studied mainly from experimental observations. The properties of the Prandtl number and pinch number were briefly compared here with theoretical predictions and a general statement on the status of momentum transport was made. The experimental observations are qualitatively consistent with the theoretical predictions in the presence of the ITG mode. In order to understand momentum transport, in other words to make a predictive modelling, detailed quantitative comparison with experiments will be needed.

A general discussion on the similarities of χ_ϕ and V_{pinch} profiles is made in section 3. The effect of the torque and heat deposition profiles on the momentum transport coefficient profiles would be worth studying for a more detailed comparison.

6. Summary

A database of momentum transport has been constructed comprising data from five tokamaks, Alcator C-Mod, DIII-D, JET, JT-60U and NSTX, to assess the characteristics of momentum transport coefficients: the momentum diffusivity (χ_ϕ) and the pinch velocity (V_{pinch}). A total of 68 discharges, 254 data points, including L- and H-mode plasmas, have been collected. The data cover a wide region of plasma parameters, such as $I_p = 0.7$–2.5 MA, $B_T = 0.4$–5.5 T, $\bar{n}_e = 1.2 \times 10^{19}$– 2.6×10^{20} m^{-3} and $P_{ABS} = 0.5$–22 MW.

Using the momentum database, the properties of momentum transport in H-mode plasmas have been investigated. Correlations between χ_ϕ and χ_i, χ_ϕ and V_{pinch} in the machines have been found; χ_ϕ increases with increasing χ_i in JET, JT-60U and NSTX, and $-V_{pinch}$ increases with increasing χ_ϕ in DIII-D, JET, JT-60U and NSTX. These correlations are observed over a wide range of χ_ϕ and RV_{pinch} at a fixed radius ($r/a = 0.6$) covering roughly two orders of magnitude, and for each of the machines over the whole radius. While χ_ϕ can vary by one order of magnitude radially, χ_ϕ/χ_i varies only by a factor of $\approx$1.5–5 in the region $r/a = 0.3$– 0.6 on JET and JT-60U. Parametric dependences of χ_ϕ/χ_i and RV_{pinch}/χ_ϕ at $r/a = 0.6$ are investigated using dimensionless parameters. Overall, χ_ϕ/χ_i tends to increase with decreasing ν_e^* at fixed ρ_{pol}^* and T_e/T_i. The ratio $-RV_{pinch}/\chi_\phi$ tends to increase with increasing R/L_{n_e} at a fixed q_{95}, which is qualitatively consistent with the theoretical prediction from the gyro-kinetic calculations [27] and observations in JET [24]. These results suggest the important role of ITG-like turbulence in driving momentum transport.

Appendix A.

A.1. Methodology

In Alcator C-Mod, χ_ϕ and V_{pinch} are evaluated in terms of the evolution of the toroidal rotation velocity profile at L–H and H–L transitions using a simple source-free momentum transport model [15]:

$$\frac{\partial}{\partial t} m_i n_i V_\phi + \frac{1}{r}\frac{\partial}{\partial r} r \left\{ -\chi_\phi \frac{\partial}{\partial r} m_i n_i V_\phi - V_{pinch} m_i n_i V_\phi \frac{r}{a} \right\} = 0. \tag{A1}$$

Here m_i, n_i, a and V_ϕ are the ion mass, ion density, minor radius and the toroidal rotation velocity, respectively. The momentum transport coefficients, χ_ϕ and V_{pinch}, are free parameters to be determined. The source of the momentum due to the L–H transition was located in the plasma edge, and the boundary conditions of an edge rotation changed from 0 to V_0 at the L–H transition. The values of χ_ϕ and V_{pinch} are determined by reproducing the time evolution of the measured toroidal rotation velocity profile through equation (A1) assuming that the ion density profile is flat and χ_ϕ and V_{pinch} are spatially and temporally constant. The electron density rose during the L–H transition maintaining a flat profile. This means that the amplitude of the modulated part of density was flat and the phase delay of the modulated part of density was also flat. In this case, the effect of the density evolution on the transient momentum transport analysis is negligible.

In DIII-D, χ_ϕ and V_{pinch} are inferred from angular momentum balance,

$$\Gamma = -m_i n_i R \chi_\phi \frac{\partial V_\phi}{\partial r} + m_i n_i R V_{pinch} V_\phi, \tag{A2}$$

in TRANSP [33] during the rotation relaxation following the NB blip perturbations [22]. Here Γ and R are the angular momentum flux in the toroidal direction and the major radius, respectively. The NB blip is 50 ms long, which is short compared with the energy confinement time. The torque profile deposited by the NB blip is calculated using the NUBEAM [34, 35] package within TRANSP. Time-invariant profiles for χ_ϕ and V_{pinch}, which best reproduce the measured V_ϕ following the NB blip perturbations, are evaluated using a non-linear least-squares fitting [35]. In the perturbation experiments, the effective torque associated with intrinsic rotation was not significantly changed and the NRMF torque [36, 37] modulation was at least a factor of 4–5 smaller than that from the torque from NB blips.

In JET, χ_ϕ and V_{pinch} are determined from time-dependent transport modelling through NBI modulation experiment [19, 23]:

$$M = -\chi_\phi m_i n_i \frac{\partial V_\phi}{\partial r} + V_{pinch} V_\phi m_i n_i. \quad (A3)$$

Here M is the momentum flux in the toroidal direction. The tangential NBI power and torque are modulated with a frequency of 6.25 Hz. The NBI-induced torque, which consists of collisional and $j \times B$ torques [38–40], is calculated with the NUBEAM code inside the TRANSP code. Profiles of χ_ϕ/χ_i (Prandtl number) and V_{pinch}, where the heat diffusivity (χ_i) is evaluated by the steady-state power balance equation, are simulated to reproduce the experimental phase and amplitude of the modulated toroidal rotation velocity. The steady state of toroidal rotation is also simulated as a third constraint, on top of amplitude and phase. H-mode plasmas with type-III ELMs at low collisionality and high q_{95} to avoid sawteeth were chosen to perform the cleanest possible rotation modulation.

In NSTX, perturbation experiments, which can yield χ_ϕ and V_{pinch}, were performed using NB pulses (200 ms, $P_{NB} = 4$ MW) and/or non-resonant $n = 3$ magnetic field pulses (40–50 ms) [20, 21]. The momentum flux including both a diffusive and a pinch term is written as equation (A2). The momentum transport coefficients, χ_ϕ and V_{pinch}, are modelled by assuming they are constant in time during the analysis period, and solving equation (A2) using a non-linear least-squares fit similar to the methodology in DIII-D [22]. The beam-driven torque profile is calculated using the NUBEAM [34, 35] package within TRANSP [33]. The non-resonant $n = 3$ magnetic perturbation results in a braking of the plasma rotation due to neoclassical toroidal viscosity (NTV) [36, 37]. The perturbation was applied for 40–50 ms, which was shorter than the energy confinement time, and much shorter than the momentum confinement time. In this case, the perturbation was non-perturbative for the energy transport properties of the plasma. The perturbation was most significant for $r/a > 0.5$ and could be seen as far as $r/a = 0.25$. The transport coefficients were determined from the time-dependent changes of the velocity and velocity gradient after the $n = 3$ perturbation was turned off.

In JT-60U, the perturbation technique with perpendicular NBs, which enhances the rotation in the counter-current direction by the fast ion losses due to the toroidal field ripple in the peripheral region, is used [16]. The values of χ_ϕ and V_{pinch}
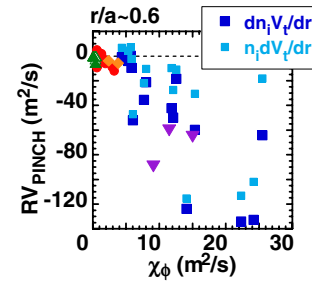
Figure 11. JT-60U data of figure 6(*b*), the same colour scheme, with the $r/a = 0.6$ data recalculated with equation (3) of the pinch velocity (V_{pinch}) as light blue squares.

are evaluated through the modulated part of the momentum balance equation [17, 18],

$$\frac{\partial m_i n_i V_\phi}{\partial t} = -\nabla \cdot \left\{ -\chi_\phi \frac{\partial m_i n_i V_\phi}{\partial r} + V_{pinch} m_i n_i V_\phi \right\} + S, \quad (A4)$$

where S is the momentum source. The amplitude of the modulated part of V_ϕ and the modulation frequency are measured, and the time-independent solutions of χ_ϕ and V_{pinch} are calculated from the perturbed component of equation (A4). The momentum balance equation is solved using a cylindrical model for toroidal momentum with flux surface averaged parameters.

A.2. Treatment of density profile in the momentum balance equation

As mentioned in section 2, the treatment of the density profile in the momentum balance equation is different in different machines. Alcator C-Mod, DIII-D, NSTX and JET take the density outside of the gradient in the momentum balance equation. JT-60U treats the density inside of the gradient. The difference ($\partial n_i V_\phi/\partial r$ or $n_i \partial V_\phi/\partial r$) does not make a difference in χ_ϕ; however, V_{pinch} can vary as discussed below.

Once again, the modulated part of the momentum balance equation taking the density inside of the gradient (from equation (2)) is given by

$$n_i \frac{\partial m_i \tilde{V}_\phi}{\partial t} = -\nabla \cdot \left\{ -\chi_\phi \frac{\partial m_i n_i \tilde{V}_\phi}{\partial r} + V_{pinch} m_i n_i \tilde{V}_\phi \right\} + \tilde{S}, \quad (A5)$$

where n_i and $\tilde{V}_\phi$ are, respectively, the time invariant terms of the ion density and the perturbed time-dependent term of the toroidal rotation velocity. Here the perturbed time-dependent term of the ion density is assumed to be negligibly small (i.e. $n_i \tilde{V}_\phi \gg \tilde{n}_i V_\phi, \tilde{n}_i \tilde{V}_t$).

Equation (A5) can be expressed by

$$n_i \frac{\partial m_i \tilde{V}_\phi}{\partial t} = -\nabla \cdot \left\{ -\chi_\phi n_i \frac{\partial m_i \tilde{V}_\phi}{\partial r} \right.$$
$$\left. + \left(V_{pinch} - \chi_\phi \frac{1}{n_i} \frac{\partial n_i}{\partial r} \right) m_i n_i \tilde{V}_\phi \right\} + \tilde{S}. \quad (A6)$$

On the other hand, the equation taking the density outside of the gradient (from equation (3)) is given by

$$n_i \frac{\partial m_i \tilde{V}_\phi}{\partial t} = -\nabla \cdot \left\{ -\chi_\phi n_i \frac{\partial m_i \tilde{V}_\phi}{\partial r} + V_{pinch} m_i n_i \tilde{V}_\phi \right\} + \tilde{S}. \quad (A7)$$

One can see that the calculated values of V_{pinch} from equations (A6) and (A7) are different when the density profile is not flat.

Figure 11 shows the recalculated V_{pinch} for the JT-60U data using equation (3). The difference in V_{pinch} ranges from 1.4 to 13 m s^{-1}, and the mean value and the standard deviation of the difference in V_{pinch} are 5.0 and 3.6, respectively. Although the value of V_{pinch} varies, the tendency or V_{pinch} increasing with increasing χ_ϕ is still observed.

References

[1] Burrell K. 1997 *Phys. Plasmas* **4** 1499
[2] Synakowski E.J. *et al* 1999 *Nucl. Fusion* **39** 1733
[3] Sakamoto Y. *et al* 2001 *Nucl. Fusion* **41** 865
[4] Wolf R.C. 2003 *Plasma Phys. Control. Fusion* **45** R1
[5] Wade M.R. for the DIII-D Team 2007 *Nucl. Fusion* **47** S543
[6] Gohil P. *et al* 2008 *J. Phys.: Conf. Ser.* **123** 012017
[7] Ward D.J. *et al* 1995 *Phys. Plasmas* **2** 1570
[8] Strait E.J. *et al* 1995 *Phys. Rev. Lett.* **74** 2483
[9] Menard J.E. *et al* 2005 *Nucl. Fusion* **45** 539
[10] Takechi M. *et al* 2007 *Phys. Rev. Lett.* **98** 055002
[11] Nakano T. *et al* 2009 *Nucl. Fusion* **49** 115024
[12] Hoshino K. *et al* 2010 *Contrib. Plasma Phys.* **50** 386
[13] Nagashima K. *et al* 1994 *Nucl. Fusion* **34** 449
[14] Ida K. *et al* 1995 *Phys. Rev. Lett.* **74** 1990
[15] Lee W.D. *et al* 2003 *Phys. Rev. Lett.* **91** 205003
[16] Yoshida M. *et al* 2006 *Plasma Phys. Control. Fusion* **48** 1673
[17] Yoshida M. *et al* 2007 *Nucl. Fusion* **47** 856
[18] Yoshida M. *et al* 2009 *Nucl. Fusion* **49** 115028
[19] Tala T. *et al* 2007 *Plasma Phys. Control. Fusion* **49** B291
[20] Solomon W.A. *et al* 2008 *Phys. Rev. Lett.* **101** 065004
[21] Kaye S.M. *et al* 2009 *Nucl. Fusion* **49** 045010
[22] Solomon W.M. *et al* 2009 *Nucl. Fusion* **49** 085005
[23] Tala T. *et al* 2009 *Phys. Rev. Lett.* **102** 075001
[24] Tala T. *et al* 2011 *Nucl. Fusion* **51** 123002
[25] Hinton F.L. and Wong S.K. 1985 *Phys. Fluids* **28** 3082
[26] Mattor N. and Diamond P.H. 1988 *Phys. Fluids* **31** 1180
[27] Peeters A.G. *et al* 2007 *Phys. Rev. Lett.* **98** 265003
[28] Hahm T.S. *et al* 2008 *Phys. Plasmas* **15** 055902
[29] Peeters A.G. *et al* 2009 *Phys. Plasmas* **16** 042310
[30] Diamond P.H. *et al* 2009 *Nucl. Fusion* **49** 045002
[31] Kluy N. *et al* 2009 *Phys. Plasmas* **16** 122302
[32] Doyle E.J. *et al* 2007 Progress in the ITER Physics Basis Chapter 2: Plasma confinement and transport *Nucl. Fusion* **47** S18
[33] Hawryluk R. 1980 *Physics Plasmas Close to Thermonuclear Conditions* vol 1, ed B. Coppi *et al* (Brussels: CEC) pp 19–46
[34] Goldston R.J. *et al* 1981 *J. Comput. Phys.* **43** 61
[35] Pankin A. *et al* 2004 *Comput. Phys. Commun.* **159** 157
[36] Shaing K.C. 2003 *Phys. Plasmas* **10** 1443
[37] Cole A.J. *et al* 2008 *Phys. Plasmas* **15** 056102
[38] Goldston R.J. *et al* 1981 *Phys. Rev. Lett.* **47** 647
[39] Salmi A. *et al* 2008 *Contrib. Plasma Phys.* **48** 77
[40] Honda M. *et al* 2009 *Nucl. Fusion* **49** 035009
[41] Gurcan O.D. *et al* 2007 *Phys. Plasmas* **14** 042306
[42] Rice J.E. *et al* 2011 *Phys. Rev. Lett.* **106** 215001
[43] Yushmanov P.N. *et al* 1990 *Nucl. Fusion* **30** 1999